

Frictional Heating and Neutron Star Thermal Evolution

Kenneth A. Van Riper, Bennett Link¹, and Richard I. Epstein
Los Alamos National Laboratory, Los Alamos, NM 87545, USA

ABSTRACT

Differential rotation between the neutron star crust and a more rapidly rotating interior superfluid leads to frictional heating that affects the star's long-term thermal evolution and resulting surface emission. The frictional heating rate is determined by the mobility of the vortex lines that thread the rotating superfluid and pin to the inner crust lattice. If vortex pinning is relatively strong, a large velocity difference develops between the inner crust superfluid and the crust, leading to a high rate of heat generation by friction. Here we present the results of thermal evolution simulations based on two models of the vortex pinning forces that bracket a range of plausible pinning strengths. We include the effects of superfluidity, magnetic fields, and temperature gradients. As representative standard and accelerated neutrino emission processes taking place in the core, we consider the modified Urca process in normal baryonic matter, and the much faster quark Urca process. Comparison of our results with neutron star surface temperature data, including the recent temperature measurement of the Geminga pulsar, shows that stars with soft equations of state and modest frictional heating are in closest agreement with the data; stars with stronger frictional heating have temperatures inconsistent with the upper limit of PSR 1929+10. Stiffer stars undergoing standard cooling generally have temperatures lying above the Vela detection, a situation worsened by the inclusion of frictional heating. Stars undergoing accelerated cooling without frictional heating have temperatures that fall far below most temperature measurements; the Vela and Geminga detections being the most compelling examples. Only in stiff stars, which have thick crusts, can the inclusion of strong frictional heating raise the temperature at late stages in the evolution to a level consistent with the data. However, such a large amount of heating leads to a temperature at ~ 1000 yr in excess of the Crab upper limit. Suppression of accelerated neutrino emission processes, perhaps by superfluid pairing in the core, may yield acceptable cooling models.

Subject headings: stars: evolution — stars: interiors — stars: neutron — stars: X-rays — dense matter

¹Also Department of Physics, Montana State University, Bozeman, Montana 59717.

1. INTRODUCTION

The study of neutron star thermal evolution affords a means of probing the properties of dense matter. A newborn neutron star is very hot, with a temperature well above an MeV. The star cools initially through neutrino emission, and later (after $\sim 10^4$ yr) cools primarily through the emission of photons from the surface. The neutrino emission process occurring in the core depends on the state of matter there. In a core composed of normal baryons, neutrino emission can occur through the relatively slow modified Urca process (“standard” cooling), or, if the core proton fraction is high enough, through the much faster direct Urca process (“accelerated” cooling). Possible states of the core include condensed pions or kaons, bulk quark matter, or hyperon-rich matter; neutrino emission processes in each of these possible states would have accelerated rates comparable to the direct Urca process. Superfluid pairing of the nucleons is expected to occur below temperatures of ~ 1 MeV, and could have a dramatic effect on neutron star thermal evolution by reducing the matter’s specific heat, and, depending on the core emission processes that actually occur, the neutrino emissivity. Furthermore, the presence of a neutron superfluid in the inner crust would lead to frictional heating, possibly raising the star’s surface temperature significantly.

Generally, stellar evolution models simulating standard cooling (*i.e.*, dominated by the modified Urca process) based on moderately stiff to very stiff equations of state predict surface temperatures greater than observed; whereas models simulating the accelerated neutrino emission from an exotic or proton-rich core predict late-time surface temperatures that are far too low (see *e.g.*, Friman & Maxwell 1979 and Van Riper 1991). Internal heating, associated with friction between the normal matter of the inner crust and a more rapidly rotating neutron superfluid, might allow agreement with data for models involving accelerated cooling, while exacerbating the problem in models of standard cooling.

Frictional heating has been examined by several authors. Alpar *et al.* (1987) assumed an approximate balance between frictional heating and photon emission from the stellar surface, and compared the predicted surface temperature with the EXOSAT upper limit on the temperature for PSR 1929+10; they concluded that only a small degree of frictional heating is allowed. Shibazaki & Lamb (1989) explored the effects of internal heating on the thermal evolution of isothermal stars older than 10^3 yr, including possible magnetic field evolution. Taking the internal heating rate as a free parameter, they compared their results with EINSTEIN and EXOSAT detections and upper limits. They found standard cooling in a stiff star to be inconsistent with the Vela detection, and consistent with other pulsars for various values of the heating rate. Accelerated cooling was found to predict temperatures falling below the surface temperatures of several pulsars, even for unrealistically high heating rates. Van Riper (1991a) considered constant internal energy sources, as would occur for steady state frictional heating, in nonisothermal neutron stars. Van Riper, Epstein, & Miller (1991) showed that the heat generated during a pulsar glitch could raise the stellar surface temperature over time scales of hours to months. Umeda, Shibazaki, Nomoto, & Tsuruta *et al.* (1993, hereafter USNT) used the parametrized heating rate of Shibazaki &

Lamb (1989) in nonisothermal simulations, and compared their results with ROSAT data that has recently become available. They found that standard cooling in stiff to medium stars gives temperatures that exceed those of PSR 0656+14 and Vela. Moreover, strong heating in a stiff star was ruled out by PSR 1055-52, and possibly by the PSR 1929+10 upper limit. The study of USNT is the most complete investigation to date, and we compare our results to theirs below.

The purpose of our study is to consider the consequences of inner crust frictional heating on neutron star thermal evolution by using a microscopic description of the superfluid coupling to the crust, rather than a parametrized form. In our analysis we use the most recent ROSAT data of cooling neutron stars, including the Geminga pulsar detection. We investigate a standard cooling model in which the modified Urca process on nucleons is the dominant cooling process in the core. As an example of an accelerated emission mechanism, we consider the quark Urca process. Much recent work has focused on the microscopic physics determining the coupling between the inner crust superfluid and the rest of the star (Alpar 1977; Pines *et al.* 1980; Alpar *et al.* 1984; Epstein & Baym 1988; Bildsten & Epstein 1989; Link & Epstein 1991, hereafter LE; Link, Epstein, & Baym 1993, hereafter LEB; Chau & Cheng 1993a, 1993b). In this study, we examine internal heating using the microscopic description for the neutron superfluid dynamics developed in LE and LEB. In this theory, the frictional heating rate depends on the stellar temperature and the strength of the interactions that pin superfluid vortex lines to the stellar crust.

Our simulations show that accelerated cooling with frictional heating is inconsistent with the data for both young and old pulsars; internal heating occurring at a rate consistent with the temperatures of old pulsars produces overheating in the early states of evolution. Standard cooling with modest frictional heating of a very soft star (*i.e.*, with a maximum mass of near $1.4 M_{\odot}$) is marginally consistent with all current temperature data. Stronger frictional heating produces a temperature at the age of PSR 1929+10 in excess of the upper limit for that pulsar.

This paper is organized as follows. In §2 we discuss the input physics of our models; we derive the frictional heating rate, and describe the two vortex pinning models used. In §3 we describe our numerical simulations. We compare our results with those of other authors and with data from the EINSTEIN, EXOSAT and ROSAT satellites in §4, and in §5 we present our conclusions. Appendix A gives the vortex creep equations from the theory of LEB. Appendix B contains a comparison of our time-dependent source calculations with simulations of cooling with time-independent sources.

2. INPUT PHYSICS

2.1. Cooling Processes

A neutron star cools by neutrino emission from the interior and photon emission from the surface. During the first 10^4 to 10^6 years, the star cools mainly through neutrino emission. Later,

surface photon radiation dominates. The neutrino cooling rate of a neutron star is determined by the unknown state of matter in the core. Depending on the mass of the star and the properties of matter at several times nuclear density, nuclear matter may extend to the center of the star, or there may exist a distinct inner core consisting of a pion or kaon condensate, hyperon-rich matter, bulk quark matter, or some other exotic state. In standard cooling models, the neutrino emission is mainly through the modified Urca process taking place in the core. Later, neutrino bremsstrahlung in the inner crust may be important, though Pethick & Thorsson (1994) argue that band structure effects suppress this process. Neutrino bremsstrahlung processes in the core also contribute to the emission. In contrast with standard models, in accelerated cooling models neutrino emissivities are orders of magnitude larger. A number of plausible accelerated cooling mechanisms have been discussed, including, the direct Urca process on nucleons in a proton-rich core, free quarks, pions, or kaons. We summarize these neutrino processes in Table 1.

2.2. Superfluid Effects

Calculations of critical temperatures for nucleon pairing (see, *e. g.*, Hoffberg *et al.* 1970; Chao, Clark, & Yang 1972; Ainsworth, Pines, & Wambach 1989; Wambach, Ainsworth, & Pines 1991) indicate that neutron stars form superfluids in their interiors shortly after their formation. In the inner crust, above the drip density of $4 \times 10^{11} \text{ g cm}^{-3}$, free neutrons form a 1S_0 superfluid which flows through a lattice of neutron-rich nuclei. At or below nuclear density, $\rho_o = 2.8 \times 10^{14} \text{ g cm}^{-3}$, the nuclei dissolve, forming a 3P_2 neutron superfluid, plus a dilute plasma of superconducting protons and normal electrons. (Recent work by Lorenz, Ravenhall, & Pethick [1993] and Lattimer & Swesty [1991] suggests nuclei dissolve at a lower density, $0.6\rho_o$.) Superfluid may or may not extend to the center of the star.

Neutrino Emission and the Specific Heat: Superfluidity reduces the phase space volume available for excitations. Consequently, both the specific heat of the paired component, and any neutrino emission process that involves nucleons (see Table 1), would be suppressed. The direct Urca process on quarks would be unaffected, unless the quarks become superfluid. The possibility of quark pairing is unresolved; in this study we assume that quark superfluidity does not occur and there is no suppression of the quark Urca process.

Frictional Heating: Friction between the normal matter of the star and a more rapidly rotating interior superfluid leads to heat generation which affects the star’s thermal evolution. The strength and time-dependence of the heat generation depends on the microscopic physics of the interaction between the superfluid and the normal matter. We now turn to a discussion of this interaction, and derive the heating rate.

The angular momentum of the rotating neutron superfluid resides in a velocity field containing singular regions of vorticity or *vortex lines*. The superfluid angular momentum is determined by

the density and distribution of these vortex lines, and can change only if they move relative to the star’s rotation axis. Were the vortex lines immobilized, by the pinning process discussed below for example, the superfluid angular momentum would remain fixed. The rotational dynamics of the superfluid, and hence, the heating associated with the coupling between the superfluid and the crust, is determined by the motion of vortex lines.

In early studies of neutron star thermal and rotational evolution, the core superfluid was assumed to be weakly coupled to the crust (Baym *et al.* 1969; Greenstein 1975; Harding, Guyer, & Greenstein 1978). However, subsequent investigations of neutron star spin fluctuations showed that at least 70% of the total moment of inertia of a neutron star is strongly coupled to the crust on time scales of greater than three days (Boynton & Deeter 1979; Boynton 1981). Theoretical studies suggest that the entire core is strongly coupled to the crust (Alpar, Langer, & Sauls 1984). Superconducting protons become entrained in the neutron circulation about a vortex, resulting in a supercurrent and an associated vortex magnetization. Electrons scatter efficiently off the vortex magnetic field, bringing the velocity between the core neutron superfluid and the charged component of the star into corotation over time scales of $\sim 10^2 - 10^4$ rotation periods (Alpar & Sauls 1988). On longer time scales, the core, which accounts for at least 90% of the total moment of inertia is tightly coupled to the crust.

Unlike the core, the inner crust neutron superfluid, which makes up $< 10\%$ of the total moment of inertia, is only weakly coupled to the crust, allowing an angular velocity difference to develop between the superfluid and the crust as the pulsar spins down. Friction between the two components produces heat. The heating may occur steadily, if the superfluid and the crust slow at nearly the same rate, or suddenly, in a glitch.

We now derive the internal heating rate in terms of the velocity difference between the superfluid and the rest of the star. As the star slows under an external torque N_{ext} , the angular momentum of the inner crust superfluid, J_s , changes according to

$$I_c \dot{\Omega}_c + \dot{J}_s = N_{\text{ext}} \equiv -I |\dot{\Omega}_\infty|, \quad (1)$$

where I_c is the moment of inertia of the solid crust and the corotating core, Ω_c is the spin rate of the crust, I is the total moment of inertia, and an overdot denotes a time derivative. The angular momentum of the inner crust superfluid in the Newtonian approximation is

$$J_s(t) = \int d^3r \rho_s(r) r_p v_s(\vec{r}, t), \quad (2)$$

where r_p is the distance from the rotation axis, ρ_s is the superfluid mass density, and v_s is the superfluid velocity, related to the angular velocity by $v_s(\vec{r}, t) = r_p \Omega_s(\vec{r}, t)$. The superfluid velocity changes as vortices move radially. Over evolutionary time scales, the superfluid and the crust remain close to rotational equilibrium such that $\dot{\Omega}_s = \dot{\Omega}_c = \dot{\Omega}_\infty$.

The total frictional heating rate is given by the rate of change of the total rotational energy

of the star, minus the rate at which work is done by the external torque:

$$H(t) = -\frac{d}{dt} \left[\frac{1}{2} I_c \Omega_c^2 + \frac{1}{2} \int \rho_s v_s(\vec{r})^2 d^3 r \right] - |N_{\text{ext}}| \Omega_c = |\dot{\Omega}_c| \int \rho_s(r) r_p^2 (\Omega_s(\vec{r}) - \Omega_c) d^3 r, \quad (3)$$

where we have used eqs. (1) and (2) to obtain the final form. The integrand, which represents the heating rate per unit volume, is greatest near the equator and falls off near the rotational poles where r_p vanishes. As we discuss below, the lag velocity between the superfluid and the crust, $\Delta v = r_p(\Omega_s - \Omega_c)$, is nearly constant on spherical shells, except near the poles. Since we are studying the thermal evolution with a one-dimensional computer code, we average the superfluid heating on spherical shells to obtain

$$H(t) = \pi^2 |\dot{\Omega}_c| \int dr \rho_s(r) r^3 \Delta v = |\dot{\Omega}_c| \int \omega_{\text{eff}} dI \equiv J_{\text{eff}} |\dot{\Omega}_c|, \quad (4)$$

where $\omega_{\text{eff}} = 3\pi\Delta v/8r$ is the effective lag frequency and $dI = (4\pi/3)\rho_s(r)r^4 dr$ is the Newtonian approximation to the moment of inertia of a shell. This expression for the total heating rate is useful for comparison with the results of Shibizaki & Lamb (1989) and USNT, who write the heating rate in this form. In our thermal evolution calculations, which allow for temperature gradients, we calculate the local heating rate in each zone, properly weighted by the moment of inertia with the general relativistic correction.

The spin rate and its time-derivative are needed in the evaluation of the heating rate. We assume a magnetic dipole spin evolution,

$$\dot{\Omega}_c(t) = -K\Omega_c^3, \quad (5)$$

where K is a positive constant. Integrating eq. (5) from a birth spin rate $\Omega_c(0) = \Omega_0$ to $\Omega_c(t)$ gives

$$\Omega_c(t) = \frac{\Omega_0}{\sqrt{1 + 2K\Omega_0^2 t}}. \quad (6)$$

For times such that $\Omega_c(t) \ll \Omega_0$, eq. (6) simplifies to

$$\Omega_c(t) = (2Kt)^{-1/2} \equiv 190h \left(\frac{t}{10^3 \text{ yr}} \right)^{-1/2} \text{ s}^{-1}, \quad (7)$$

where we have chosen a fiducial value of the constant K that gives a spin down rate that is typical of the pulsars examined in this study. Each pulsar's spin evolution is characterized by a value of h (see Table 2). For the numerical solutions presented below, we use $h = 1$. For a birth period of ~ 1 ms, eq. (7) is a good approximation after ~ 10 yr.

The velocity lag appearing in the expression for the heating rate (eq. [4]) is determined by the vortex mobility, since only if vortices move radially can the superfluid velocity change. Interaction forces between vortices and nuclei, however, tend to *pin* vortices to the lattice. At high densities, above $\sim 10^{13}$ g cm $^{-3}$, the vortex–nucleus interaction is attractive, and vortices pin strongly to

nuclei (Alpar 1977; Epstein & Baym 1988). At lower densities, the interaction is repulsive, and vortices pin weakly to the interstices of the lattice (Epstein & Baym 1988; LEB). In either region, vortex pinning tends to maintain a local superfluid rotational velocity that is higher than that of the crust. Following LEB, we consider the motion of vortices by the process of *vortex creep*, which proceeds by thermal or quantum activation of the vortices over their pinning barriers. Other mechanisms for moving vortex lines have been discussed. For example, Ruderman (1976; 1991) argues that in regions where vortex pinning is sufficiently strong, the crust may crack before the vortices unpin, and plates of crustal material will carry vortices toward the stellar equator. Jones (1990) has suggested that vortex pinning never occurs and that the superfluid remains in a state of near corotation with the crust. In LEB it was shown, however, that a vortex line adjusts its configuration in such a way as to be much more strongly pinned than Jones estimated.

In this investigation, we assume that vortex creep allows the superfluid to slow at the same steady rate as the crust. Steady-state vortex creep, however, cannot account for all aspects of pulsar timing, especially the observed glitches in spin rate. Glitches are thought to reflect sudden transfers of angular momentum from the neutron superfluid to the crust. Some pulsars, *e.g.* the Vela pulsar, lose angular momentum mainly during glitches, rather than through steady vortex creep. In such cases, steady-state vortex creep is never achieved and the mean frictional heating rate is smaller than we calculate here.

From vortex number conservation, the equation of motion for the superfluid is (see, *e.g.*, LEB)

$$\dot{\Omega}_s(\vec{r}, t) \simeq \frac{-2\Omega_s(\vec{r}, t)}{r_p} v_{cr}(\vec{r}, t). \quad (8)$$

where $v_{cr}(\vec{r}, t)$ is the radial vortex creep rate. In eq. (8) we have neglected gradients in Ω_s , which are small in the inner crust. We consider cases such that $|\Omega_s - \Omega_c| \ll \Omega_c$, and fix $\dot{\Omega}_s(\vec{r}, t) = \dot{\Omega}_c$ in eq. (8) to obtain

$$v_{cr}(\vec{r}, t) \simeq -r_p \frac{\dot{\Omega}_c}{2\Omega_c}. \quad (9)$$

The vortex creep rate has the general form

$$v_{cr} = v_0 e^{-A/T_{\text{eff}}}, \quad (10)$$

where v_0 is a microscopic velocity, A is the activation energy for a segment of vortex line to overcome its pinning barrier, and T_{eff} is the effective temperature and which differs from the stellar value at low temperatures because of quantum effects. The LEB result for the vortex creep rate is summarized in Appendix A. The activation energy depends sensitively on the vortex-nucleus interaction energy (which varies with the stellar density) and on the difference between the velocities of the superfluid and the crust, $\Delta v(\vec{r}) \equiv r_p(\Omega_s - \Omega_c)$. The solution of eqs. (9) and (10) for $\Delta v(\vec{r})$ depends only logarithmically on r_p , so that $\Delta v(\vec{r})$ is nearly constant on spherical shells as we assumed in obtaining eq. (4).

The strength of vortex pinning varies significantly with density in the inner crust, especially near $10^{13} \text{ g cm}^{-3}$, where the character of pinning changes from interstitial to nuclear. An

interstitially vortex samples only the long range part of the interaction, and the pinning energies are very weak (~ 1 keV). Above $\sim 10^{13}$ g cm $^{-3}$, where vortices pin directly to nuclei, the pinning energies become difficult to calculate reliably, as the vortex samples the poorly understood short-range nuclear pinning potential. We consider two models for pinning which differ in the high-density region:

- *EB* Pinning Model: LE and Epstein & Baym (1988) pinning parameters are used.
- *ACP* Pinning Model: Above $\sim 1.5 \times 10^{13}$ g cm $^{-3}$, pinning parameters are obtained in LEB from the approach of Alpar, Cheng & Pines (1989) based on the superfluid gap calculations of Ainsworth, Pines, & Wambach (1989). Elsewhere LE and Epstein & Baym (1988) pinning parameters are used.

A calculation of the pinning interaction in the nuclear pinning region requires solving the BCS equations for pairing of neutrons in the presence of flow, both inside and outside nuclei. This problem has yet to be solved. In the EB model pinning energies are estimated by using Ginzburg-Landau theory; pinning energies in this model for the high-density region of the inner crust are typically ~ 10 MeV. In the ACP model, pinning energies are estimated by simple volume arguments; pinning energies in this model are ~ 1 MeV or less.

Vortex creep will produce the most heat in the regions of nuclear pinning, since those regions have the most moment of inertia and the highest pinning energies. In the core, the velocity difference between components is negligible, and there is no significant frictional heat generation. Above $\sim 1.3 \times 10^{14}$ g cm $^{-3}$, the nuclear spacing and the characteristic vortex dimension become comparable. In this region the pinning may become “superweak”, as suggested by Alpar *et al.* (1984), or may vanish altogether as Jones (1991) argues. In either case, the heating from such regions would be small and we ignore it in this investigation.

3. SIMULATIONS

We consider neutron stars with gravitational masses of $1.4M_{\odot}$ constructed by solving the Oppenheimer-Volkoff equation for hydrostatic equilibrium based on the equations of state (EOSs) of Baym, Pethick, & Sutherland (1971; BPS; with the Pandharipande [1971] model C alternative at high density), Pandharipande & Smith (1975; PS), and Friedman & Pandharipande (1981; FP). The BPS model is representative of soft EOSs which yield stellar models with high central densities and thin, low-mass crusts. The PS model was chosen as an example of an extremely stiff model with low central density and a thick crust. The FP EOS, a representative intermediate model, results in a crust size within the range found using current models for the high density EOS (*e. g.*, Prakash, Ainsworth, & Lattimer 1988). Radii R and central densities ρ_c for $1.4M_{\odot}$

stars constructed from these EOSs are given in Table 3. As a guide for comparison with Shibazaki & Lamb (1989) and UNST, we also show the maximum superfluid excess angular momentum, $J = \int dI \omega_{\text{crit}}$, and the maximum average lag, $\bar{\omega} = \int dI \omega_{\text{crit}} / \int dI$, integrated over the pinning region for our two pinning models.

We consider two examples for the dominant core neutrino emission. In our standard cooling model, we use the modified Urca process, suppressed by superfluidity. As a specific example of accelerated neutrino emissivity, we consider the quark Urca process (Kiguchi & Sato, 1981). Electron-nucleus bremsstrahlung, the dominant neutrino emission process in the crust, is included in both cooling models.

The frictional heating rate is obtained at each timestep as follows. Using the pinning parameters given as a function of density in Table 7, eq. (9), coupled with eqs. (7) and (A1)–(A15), is solved to obtain the superfluid velocity lag as a function of the local density and temperature. We evaluate the local heating rate $|\dot{\Omega}| \omega_{\text{eff}} dI$ on a grid of spherical mass shells, where dI is the moment of inertia of each shell, with the general relativistic correction. The thermal evolution is calculated using the penta-diagonal scheme of Van Riper (1991b), which allows for thermal gradients. Evolutionary calculations of this type (see also, *e. g.*, Nomoto & Tsuruta 1987) show that isothermality is not obtained in the interior until an age of up to 10^4 yr, depending on the stellar model. Before the star becomes isothermal, the calculated luminosity can differ significantly from that found in an isothermal model. The neutrino emissivities, heat capacities, and thermal conductivities, and the details of the differencing scheme, solution algorithms, and boundary conditions are given in Van Riper (1991b).

In Figs. 1–3 we show thermal evolution of neutron stars with and without frictional heating. The right ordinates give L_∞ , the bolometric luminosity seen by a distant observer, and the left ordinates give the corresponding effective temperatures T_s^∞ . Stars with thicker crusts, as illustrated by the PS model, have greater frictional heating and correspondingly higher surface temperatures at late times than stars with thinner crusts (*e. g.*, BPS). Moreover, the EB pinning model, which leads to larger lag velocities and greater heating than the ACP model, produces larger surface temperatures. At late times the surface emission is controlled entirely by the heat source, and L_∞ decreases as $|\dot{\Omega}_c| \propto t^{-3/2}$ [see eqs. (4) and (7)]. The temperature dependence of the vortex creep rate produces order unity deviations in the heating rate from the $t^{-3/2}$ behavior, as shown in Fig. 4 (top panel). For comparison with the work of other authors, we present the scaled heating rate $H(t)t^{3/2}$ at 10^7 yr in Table 4 for different pinning models and equations of state. In Fig. 4 (bottom panel) we show the evolution of the inner crust temperature T_m . The fall in T_m after $\sim 10^3$ yr in the quark models produces a larger superfluid lag and a correspondingly larger heating rate. Comparison of our full evolutionary calculations with models that use time-independent energy generation are given in Appendix B. There we find that when significant frictional heating is present, the surface temperature is largely determined by balance between the source and the combined neutrino and photon emission, and is essentially independent of the star’s thermal history.

3.1. Comparison with USNT

USNT applied the heating formulae of Shibazaki & Lamb (1989) to thermal evolution models. Their heating is $H(t) = J|\dot{\Omega}_c|$ where J is an assumed constant differential angular momentum. For each stellar model, three values of J are considered, corresponding to “superweak”, “weak”, and “strong” pinning, where $J_{\text{strong}} = 10J_{\text{weak}} = 100J_{\text{superweak}}$. Magnetic dipole braking was assumed, giving $H \propto t^{-\frac{3}{2}}$.

The values of $J_{\text{superweak}}$, J_{strong} , and the scaled heating rate $H(t)t^{3/2}$ are listed in Table 5. USNT heating rates are plotted as a function of time in Fig. 5 for an FP star, together with our standard cooling model results. For PS stars, which have thicker crusts, our EB heating is ~ 3 times stronger than shown in Fig. 5, and for a BPS star, which has a thinner crust, the EB heating is ~ 2 times less than shown. The changes for the ACP heating among different stellar models are relatively smaller.

The results of USNT at early times (< 500 yr) differ from ours primarily because of the differing treatments of the early-time heating rate. USNT adopt a nearly constant heating rate of $< 10^{38}$ erg s $^{-1}$ for times much earlier than 300 yr. However, superfluid condensation is expected to occur in the inner crust within a year of the star’s birth, leading to substantial frictional heating at early times. Our treatment of early-time thermal evolution includes this time-dependent heating. The USNT cooling curves exhibit a small \dot{T} at early times because their relatively low heating rate cannot compete with the rapid neutrino emission. The USNT results exhibit a rapid drop in surface temperature at ~ 30 yr caused by the arrival at the surface of the cooling wave from the core, rather than by the star’s response to the changing heating rate. In our models, however, the temperature evolution has nearly zero slope at early times, when the heating and neutrino cooling rates essentially balance. The rapid drop in temperature does not occur until after ~ 100 yrs in our quark models because the initiation of the cooling wave is delayed by our larger early-time heating rate. At late times, when the thermal evolution is controlled by the same heating rate, our results are consistent with those of USNT.

4. COMPARISON WITH OBSERVATIONS

Soft x-ray emission has been detected from the surfaces of at least four neutron stars, and interesting upper limits have been obtained for numerous other objects. We now discuss the measurements, compare these data with our cooling simulations, and obtain constraints on the neutron star equation of state and internal heating source. The data are shown along with our cooling simulations in Figs. 1–3, and our results are summarized in Table 6. The interpretation of a spectrum in terms of an effective temperature T_s^∞ , or equivalently, a luminosity L_∞ , quantities we show in our figures, depends on the full spectrum of radiation emitted by the star. A first

estimate of the effective temperature could be obtained by assuming that the star radiates as a blackbody. However, the dependence of the atmospheric opacity on photon energy can lead to a substantial difference between the temperature inferred from a blackbody fit (T_{BB}) and the effective temperature. For example, in a nonmagnetic atmosphere composed of light elements, the opacity drops with photon energy in the detector bandpass. As a result, the deeper, hotter atmospheric layers are exposed at higher energies, hardening the emitted spectrum, and the effective temperature can be up to a factor of three less than T_{BB} (Romani 1987). Strong magnetic fields broaden opacity features, softening the spectrum relative to the nonmagnetic case. Differences in treatment of the polarization-dependent transport have given different results. When considering only the portion of the spectrum in the ROSAT bandpass, Miller (1992; 1993) obtains effective temperatures about equal to T_{BB} for H, He, C, and N atmospheres, while for the EINSTEIN bandpass T_{BB} can be significantly less than the effective temperature — up to a factor of 0.7 in C and N atmospheres. On the other hand, Shibano *et al.* (1993) obtain effective temperatures intermediate between Romani’s (1987) nonmagnetic values and T_{BB} . In a non-magnetic Fe atmosphere, the average soft x-ray opacity is dominated by the presence of spectral lines, the spectrum is softened relative to a light-element atmosphere, and the effective temperature is close to T_{BB} (Romani 1987). The structure of heavy elements in strong magnetic fields is poorly understood, making an assessment of the full consequences for the spectrum impossible at present, however, because magnetic fields tend to soften the spectrum it is not impossible that such an atmosphere could have an effective temperature exceeding T_{BB} . Given the above caveats, in Figs. 1–3 we show the reported effective temperatures obtained from blackbody fits.

Except for the Crab, whose age is known, we use the ages estimated from the pulsar spin down. This estimate is uncertain by at least a factor of three. For stars older than 100,000 years, varying the age within this uncertainty may, depending on the model assumed, bring the observational point above or below our cooling curves. We show an error cross in the upper right of Figs. 1–3 to represent the uncertainties in the spindown ages and in the temperatures due to differences in atmosphere models.

PSR 0656+14: The flux and spectrum over a limited band have been measured for this pulsar. From EINSTEIN observations, Córdoba *et al.* (1989) deduce T_s^∞ between 3 and 6×10^5 K. Finley, Ögelman, & Kiziloğlu (1992) obtain the spectrum with the ROSAT Position Sensitive Proportional Counter and find an effective surface black body temperature of $T_s^\infty \simeq 9.0 \pm 0.4 \times 10^5$ K. Radiation transfer in an atmosphere could have significant effects on the determination of T_s^∞ . Finley, Ögelman, & Kiziloğlu (1992) obtain $\simeq 2.4 \pm 0.2 \times 10^5$ K using the non-magnetic He atmospheric model of Romani (1987). Finley & Ögelman (1993) find $9.2 \pm 0.6 \times 10^5$ K using the magnetic ($B = 9.4 \times 10^{11}$ G) He model of Miller (1992), while Anderson, *et al.* 1993, using the magnetic ($B = 4.7 \times 10^{12}$ G) H model of Shibano *et al.* (1993), obtain $5.35 \pm 0.35 \times 10^5$ K. Complicating the interpretation even further is a 14% pulsation in the thermal X-rays, suggesting a distribution of temperature over the surface. We show the blackbody results of Finley Ögelman,

& Kiziloğlu (1992) in Figs. 1–3.

Vela (PSR 0833-45): The flux and spectrum over a limited band have been measured for this star. The EXOSAT detections (Ögelman & Zimmermann 1989), fit assuming a blackbody source spectrum, are shown in in Figs. 1–3.

PSR 1055-52: The flux and spectrum over a limited band have been measured by EXOSAT for this pulsar (Brinkmann & Ögelman 1987). We show the reported temperature error bar derived from a blackbody fit.

Geminga: Halpern & Ruderman (1993) use a two-component model to fit the ROSAT spectrum, and obtain a high-temperature component of $\sim 3 \times 10^6$ K, attributed to a polar cap, and a cooler component of $\sim 5.2 \pm 1 \times 10^5$ K, associated with the remainder of the surface. The temperature of the cooler component is shown in Figs. 1–3.

Crab (PSR 0531+21): We show an upper limit to L_∞ for the Crab pulsar obtained from recent ROSAT measurements by Becker & Aschenbach (1994). This upper limit (and that for PSR 1929+10) is plotted at the same L_∞ , rather than at the same T_s^∞ , in Figs. 1–3, reflecting the experimental limit on the flux.

PSR 1929+10: We show an upper limit to L_∞ from this pulsar obtained by Alpar, *et al.* (1987). A recent measurement by Yancopoulos, Hamilton, & Helfand (1994) gives a comparable upper limit based on the net luminosity of the star. At the time and luminosity of this limit, the cooling curves are sensitive to the surface magnetic field strength chosen. Our curves assume $B = 10^{12}$ G. The curves would reach the PSR 1929+10 luminosity more quickly, by a factor of two, were $B = 10^{13}$ assumed; $B = 10^{11}$ would increase the cooling time by a factor of two.

Other upper limits: The unlabeled short arrows in Fig. 1 are 2σ upper limits to the temperatures of radio pulsars from the ROSAT all sky survey (Becker, Trümper, & Ögelman, 1993). These points were derived from observed counting rates assuming blackbody spectra. One ROSAT upper limit, for PSR 1916+14, is labeled in the figure because it provides interesting constraints on our models.

Searches for neutron stars have proven unsuccessful in the following supernova remnants: Cas-A (Murray, *et al.* 1979), Kepler (Helfand, Chanan, & Novick 1980), Tycho (Gorenstein, Seward, & Tucker 1983), SN 1006 (Pye, *et al.* 1981), RCW 86, W28, (Helfand, Chanan, & Novick 1980), and RCW 103 (Becker, *et al.* 1993; earlier interpretation of EINSTEIN data by Touhy & Garmire [1980] suggested a point source with a temperature $T_s^\infty = 2.2 \times 10^6$ K for RCW 103.) Present luminosity upper limits on point sources in Tycho, SN 1006, and RCW 103 fall below the standard cooling results; the discovery of a neutron star in any of these remnants would be strong evidence that accelerated neutrino cooling is taking place.

5. DISCUSSION AND CONCLUSIONS

Frictional heating associated with differential rotation between the inner crust neutron superfluid and the crust could significantly affect neutron star thermal evolution, particularly at late times. Our simulations show that frictional heating keeps the surface temperature above 10^5 K for $t > 10^6$ yr, perhaps to ages as great as 10^9 yr, suggesting a population of potentially observable stars (see Figs. 1–3). Stars with small radii and soft equations of state, as illustrated by our BPS model, are in closest agreement with all the current measurements and upper limits for standard cooling with ACP frictional heating or no heating (Figs. 1–3 and Table 6). The stronger EB heating predicts a temperature at the age of PSR 1929+10 in excess of the upper limit for that pulsar. Our ACP model for a BPS star has an excess superfluid angular momentum of $\sim 3.4 \times 10^{43}$ gm cm² rad s⁻¹, corresponding to an average lag of ~ 10 rad s⁻¹. Our conclusion differs from that of Alpar et al. (1987), who conclude that the excess angular momentum must be less than $\sim 7 \times 10^{42}$ gm cm² rad s⁻¹, with a corresponding average lag of less than ~ 0.7 rad s⁻¹. Standard cooling of a BPS star lies slightly above the highest estimate for Vela’s surface temperature. However, this discrepancy is not immitigable, given the uncertainties in Vela’s age and emission spectrum. Because soft stars have thin crusts, frictional heating is less important than in stiff stars, and there is little difference between the cooling curves with EB heating, ACP heating, or no heating, except at very late times. Although soft equations of state are consistent with the neutron star surface emission, elsewhere we have argued that an equation of state as soft as BPS cannot account for pulsar post-glitch behavior (Link, Epstein, & Van Riper 1992). In addition, the maximum stable mass of a BPS star is only $1.414M_{\odot}$, which is $\sim 2\%$ lower than the mass of PSR 1913+16. A star slightly stiffer than BPS, as preferred by Brown (1988), while consistent with both pulsar glitch data and neutron star mass determinations, would increase the nominal discrepancy between the cooling curves and the Vela detection.

The Vela pulsar provides the strongest argument against standard cooling in stiffer stars, *e. g.* PS or FP, which have cooling curves lying above the Vela detection. Accelerated cooling models without heating fall below measured surface temperatures; the Vela and Geminga detections are the most compelling examples. Frictional heating lessens this disagreement, but the strongest frictional heating (*e. g.*, EB in a PS star; Fig. 3) barely brings the cooling into agreement with the Vela and Geminga detections, while lying above the Crab and PSR 1929+10 upper limits. It appears that no combination of frictional heating and accelerated cooling is consistent with current data. Lattimer *et al.* (1993) and Page (1994), however, have emphasized that accelerated cooling processes are suppressed by superfluidity. Accounting for this suppression would give cooling curves that fall between those of our quark models and our standard models, and models of this sort may be consistent with current X-ray data.

ACKNOWLEDGEMENTS

It is a pleasure to thank W. Becker, F. K. Lamb, G. Pavlov, M. C. Miller, and R. Romani for valuable discussions. This work was performed under the auspices of the U.S. Department of Energy.

APPENDIX A. VORTEX CREEP RATE

The vortex mobility is determined by the strength with which vortices pin to the lattice, and by the local velocity difference $\Delta v = r_p(\Omega_s - \Omega_c)$ between the superfluid and the crust. The pinning parameters used in this study are listed in Table 7 for selected densities: the pinning energy U_0 , the vortex coherence length ξ , the Wigner-Seitz lattice spacing l_{\min} , the normalized vortex stiffness τ/Λ , and the critical differential velocity v_B above which vortex lines cannot pin. LEB obtain the average creep velocity for vortex lines in two limits - the flexible limit ($\tau \ll 1$), in which vortex motion occurs by unpinning at one site at a time, and the stiff limit ($\tau \gg 1$), in which a vortex segment unpins j bonds simultaneously. In these limits the creep rates are given by

$$v_1 \simeq \frac{2\omega_1}{\pi} l_{\min} e^{-A_1/T_{\text{eff},1}}, \quad \text{flexible}, \quad (\text{A1})$$

$$v_j \simeq \frac{5\omega_j}{\pi} l_{\min} \left[\frac{2\pi T_{\text{eff},j}}{A_j} \right]^{1/2} e^{-A_j/T_{\text{eff},j}} \quad \text{stiff}. \quad (\text{A2})$$

The symbols in eqs. (A1) and (A2) are defined as follows:

$$A_1 = U_0 \Delta^{3/2} \quad (\text{A3})$$

$$T_{\text{eff},j} \equiv \frac{\hbar\omega_j}{2} \coth \frac{\hbar\omega_j}{2T} \quad (j \geq 1) \quad (\text{A4})$$

$$\omega_1 \simeq \frac{\pi\kappa\Lambda}{4l_{\min}^2} \quad (\text{flexible } \tau \ll 1) \quad (\text{A5})$$

$$\omega_j \simeq \frac{\Delta^{1/2}}{2\pi} \frac{\kappa\Lambda}{\tau l_{\min}^2} \left[1 + \frac{\tau\pi^2}{2(j+1)^2\Delta^{1/2}} \right] \quad (\text{stiff } \tau \gg 1) \quad (\text{A6})$$

$$\Lambda = 0.116 - \ln \left[\frac{\pi\xi}{(j+1)l_{\min}} \right], \quad (\text{A7})$$

where $\Delta \equiv 1 - \Delta v/v_B$ and $\kappa = 0.0019 \text{ cm}^2 \text{ s}^{-1}$ is the quantum of vorticity. The quantities j and A_j are given by

$$j = 3.242\tau^{1/2}\Delta^{-1/4} \quad (\text{A8})$$

$$A_j = 1.577U_0\Delta^{3/2}j, \quad (\text{A9})$$

for $\Delta < 1/4$, while for $\Delta \geq 1/4$ they are

$$j = \frac{2\sqrt{2}\tau}{\Delta^{1/4}} \left[\text{sech}^{-1}\left(\frac{1}{\sqrt{3}}\right) - \text{sech}^{-1}\chi + \frac{\Delta\psi}{\sqrt{3\mathcal{F}}} \right], \quad (\text{A10})$$

$$A_j = U_0\sqrt{\tau}\Delta^{3/4} \left[\frac{18\sqrt{2}}{5} I\Delta^{1/2} - \frac{2\Delta^{3/2}\psi^3}{6^{3/2}\mathcal{F}} + \frac{3\psi}{\sqrt{6}\mathcal{F}} \left(\frac{2}{3} - \mathcal{F} + \frac{2\Delta^{3/2}}{3} \right) \right]. \quad (\text{A11})$$

Here $\mathcal{F} \equiv \Delta v/v_B = 1 - \Delta$, and,

$$I \equiv 1 - \frac{5}{2}(1 - \chi^2)^{3/2} + \frac{3}{2}(1 - \chi^2)^{5/2}, \quad (\text{A12})$$

$$\psi \equiv \left(2 + \frac{3}{\Delta^{1/2}} - \frac{1}{\Delta^{3/2}} \right)^{1/2}, \quad (\text{A13})$$

$$\chi \equiv \left[\frac{1}{3} \left(1 + \frac{1}{\Delta^{1/2}} \right) \right]^{1/2}. \quad (\text{A14})$$

The quantities τ and j are functions of one another. In our calculations of the vortex creep steady state, these quantities are determined iteratively - a trial value of τ is chosen, j is calculated, a new value of τ is obtained, j is again calculated, etc., until convergence.

Eqs. (A1) and (A2) are for the limiting cases of $\tau \ll 1$ and $\tau \gg 1$. To account for intermediate stiffness, we interpolate between the limiting cases by using the expression

$$v_{\text{cr}} = \frac{1}{j} [(1 - j)v_j + v_1]. \quad (\text{A15})$$

APPENDIX B. COMPARISON WITH STEADY STATE SOURCE CALCULATIONS

Here we compare the results of our evolutionary calculations with those of models that assume time-independent energy generation in the crust (*e. g.*, Van Riper 1991a). We have calculated steady-state models for an inner crust source in an FP star. In Fig. 6 we plot the surface luminosity as a function of steady-state source strength. In Fig. 7 we compare the thermal evolution from our frictional heating model with the equilibrium temperature of a steady-state heating model. Each filled circle was obtained as follows: in our full evolutionary calculations we extract the heating rate at a selected time. We then perform an evolutionary calculation with this constant heating rate, until the temperature reaches a steady state. The circle represents the resulting surface luminosity. Where the circles fall on the cooling curves, heat generation balances the combined surface and neutrino emissions, and the thermal history of the star is unimportant.

Cooling curves calculated assuming an isothermal interior are shown as *dashed lines* in Figs. 6 and 7. These curves coincide with the evolutionary results for $H \leq 10^{36}$ erg s⁻¹ for both standard and accelerated cooling, indicating that the interior temperature profile is effectively isothermal. The cooling curve for the standard cooling case is above the steady state points for $10^{35} \geq H \geq 10^{32}$ erg s⁻¹ (10⁴ to 10⁶ yr). The additional radiation is residual thermal energy. For higher H , the hot crust insulates the interior from the surface and L is determined only by the heating rate in the crust (the initial heat content in the crust is negligible). The difference between the steady state and evolutionary models is greatest in our BPS model, which has relatively small heating, and is negligible for the highly heated PS star. The surface temperature of the accelerated cooling models is mainly due to the source once isothermality obtains. The heat content of the core, which has been reduced by enhanced neutrino emission, contributes only a negligible fraction to the surface luminosity. The quark model cooling curve shows a sudden decline between 100 and 1000 years, similar to the drop caused by a cooling wave reaching the surface in a star undergoing accelerated cooling with no or weak crust heating. In our strong heating case, however, the shape of the cooling curve is controlled by the time dependence of the source rather than by the dynamics of conduction in the crust.

TABLE 1
NEUTRINO EMISSION PROCESSES

Process	Emissivity ^a (erg s ⁻¹ cm ⁻³)	Reference
Direct Urca	$\begin{cases} n \rightarrow p + e^- + \bar{\nu}_e \\ p + e^- \rightarrow n + \nu_e \end{cases}$	$\sim 10^{27} T_9^6$ Lattimer et al. 1991
Modified Urca	$\begin{cases} n + n' \rightarrow n' + p + e^- + \bar{\nu}_e \\ n' + p + e^- \rightarrow n' + n + \nu_e \end{cases}$	$\sim 10^{20} T_9^8$ Friman & Maxwell 1979
Core bremsstrahlung	$\begin{cases} n + n' \rightarrow n + n' + \nu_e + \bar{\nu}_e \\ n + p \rightarrow n + p + \nu_e + \bar{\nu}_e \\ e^- + p \rightarrow e^- + p + \nu_e + \bar{\nu}_e \end{cases}$	$\sim 10^{19} T_9^8$ Friman & Maxwell 1979
Quark Urca	$\begin{cases} d \rightarrow u + e^- + \bar{\nu}_e \\ u + e^- \rightarrow d + \nu_e \end{cases}$	$\sim 10^{26} \alpha_c T_9^6$ Iwamoto 1980
Pion condensate	$\begin{cases} n + \pi^- \rightarrow n + e^- + \bar{\nu}_e \\ n + e^- \rightarrow n + \pi^- + \nu_e \end{cases}$	$\sim 10^{26} T_9^6$ Maxwell et al. 1977
Kaon condensate	$\begin{cases} n + K^- \rightarrow n + e^- + \bar{\nu}_e \\ n + e^- \rightarrow n + K^- + \nu_e \end{cases}$	$\sim 10^{24} T_9^6$ Brown et al. 1988
Crust bremsstrahlung	$e^- + (A, Z) \rightarrow e^- + (A, Z) + \nu_e + \bar{\nu}_e$	$\sim 10^{20} T_9^6$ Itoh et al. 1984

^a T_9 is the temperature in units of 10^9 K.

TABLE 2
SPIN DOWN PARAMETER

Pulsar	h
Crab	0.7
Vela	1.3
Geminga	2.6
1055-52	4
1929+10	8
0656+14	0.9
1916+14	0.3

Table 3
 $M = 1.4M_{\odot}$ NEUTRON STARS

EOS	R (km)	ρ_c (g cm $^{-3}$)	$J/10^{44}$ (g cm 2 rad s $^{-1}$)	$\bar{\omega}$ (rad s $^{-1}$)
BPS	7.34	4.89×10^{15}	$4^a/0.34^b$	$145^a/13^b$
FP	10.57	1.27×10^{15}	24/2.4	97/10
PS	15.83	4.69×10^{14}	450/19	78/3.3

^aEB model

^bACP model

TABLE 4
 HEATING RATES

EOS	GAP	$H(t)t^{3/2}$ (10 Myr) (erg s $^{1/2}$)
PS	EB	2.64×10^{42}
PS	ACP	1.27×10^{41}
FP	EB	1.50×10^{41}
FP	ACP	1.52×10^{40}
BPS	EB	2.55×10^{40}

TABLE 5
 USNT HEATING RATES

EOS Pinning †	$J/10^{44}$ (g cm 2 rad s $^{-1}$)	$H(t)t^{3/2}$ (10 Myr) (erg s $^{1/2}$)
PS/S	31.0	3.7×10^{41}
PS/SW	0.31	3.7×10^{39}
FP/S	7.3	6.4×10^{40}
FP/SW	0.073	6.4×10^{38}
BPS/S	4.8	2.9×10^{40}
BPS/SW	0.048	2.9×10^{38}

† S = strong pinning, SW = superweak pinning.

TABLE 6
ALLOWED CASES

Pulsar	Heating	Model					
		BPS	BPS(accel)	FP	FP(accel)	PS	PS(accel)
Crab	none	Y	Y	Y	Y	N	Y
	ACP	Y	Y	Y	Y	N	Y
	EB	Y	Y	N	Y	N	N
Vela	none	N	N	N	N	N	N
	ACP	N	N	N	N	N	N
	EB	N	N	N	N	N	Y
Geminga	none	Y	N	Y	N	Y	N
	ACP	Y	N	N	N	N	N
	EB	Y	N	N	N	N	Y
1055-52	none	Y	N	Y	N	N	N
	ACP	Y	N	Y	N	Y	N
	EB	Y	N	Y	N	N	N
1929+10	none	Y	Y	Y	Y	Y	Y
	ACP	Y	Y	N	N	N	N
	EB	N	N	N	N	N	N
0656+14	none	Y	N	Y	N	Y	N
	ACP	Y	N	Y	N	Y	N
	EB	Y	N	N	N	N	N
1916+14	none	Y	Y	N	Y	Y	Y
	ACP	Y	Y	N	Y	N	Y
	EB	N	Y	N	Y	N	Y

TABLE 7
NUCLEAR PINNING PARAMETERS

$\text{LOG}_{10} \rho$ (g cm^{-3})	U_0 (MeV)	ξ (fm)	l_{\min} (fm)	τ/Λ	v_B (cm s^{-1})
EB Pinning Model					
11.83	0.00066	2.6	98.	21.	1.4×10^5
11.99	0.0018	2.3	93.	20.	1.6×10^5
12.18	0.0036	2.0	89.	17.	1.9×10^5
12.41	0.0090	1.7	84.	16.	2.1×10^5
12.79	0.025	1.5	79.	13.	2.7×10^5
12.98	0.4	1.4	71.	0.053	1.6×10^7
13.18	6.4	1.5	66.	0.0068	1.6×10^8
13.53	15.0	1.9	57.	0.009	3.8×10^7
13.89	9.0	4.6	39.	0.070	1.7×10^8
14.12	5.4	18.	29.	0.12	5.2×10^7
ACP Pinning Model					
11.83	0.00066	2.6	98.	21.	1.4×10^5
11.99	0.0018	2.3	93.	20.	1.6×10^5
12.18	0.0036	2.0	89.	17.	1.9×10^5
12.41	0.0090	1.7	84.	16.	2.1×10^5
12.79	0.025	1.5	79.	13.	2.7×10^5
12.98	0.4	1.4	71.	0.053	1.6×10^7
13.18	6.4	1.5	66.	0.0068	1.6×10^8
13.53	1.0	7.9	57.	0.22	8.0×10^6
13.89	0.97	12.	39.	1.8	3.2×10^6
14.12	0.22	30.	29.	110.	2.4×10^5

REFERENCES

- Ainsworth, T., Pines, D., & Wambach, J. 1989, *Phys. Lett. B*, 222, 173.
- Alpar, M. A. 1977, *ApJ*, 213, 527.
- Alpar, M. A., Anderson, P.W., Pines, D. & Shaham, J. 1984, *ApJ*, 276, 325.
- Alpar, M. A., Brinkmann, W., Kiziloğlu, Ü., & Ögelman, H. 1987, *A&A*, 177, 101.
- Alpar, M. A., Cheng, K. S., & Pines, D. 1989, *ApJ*, 346, 823.
- Alpar, M. A., Langer, S. A., & Sauls, J. A. 1984, *ApJ*, 282, 533.
- Alpar, M. A. & Sauls, J. A. 1988, *ApJ*, 327, 723.
- Anderson, P. W., & Itoh, N. 1975, *Nature*, 256, 25.
- Anderson, S. B., Córdoba, F. A., Pavlov, G. G., Robinson, C. R., & Thompson, Jr., R. J. 1993, *ApJ*, 414, 867.
- Baym, G., Pethick, C. J., Pines, D., & Ruderman, M. A. 1969, *Nature*, 224, 872.
- Baym, G., Pethick, C., & Sutherland, P. 1971, *ApJ*, 170, 299 (BPS).
- Becker, W. & Aschenbach, B. 1994, *Lives of the Neutron Stars*, Eds. A. Alpar, Kiziloğlu, Ü., & van Paradijs, J. (Kluwer), in press.
- Becker, W., Trümper, J., Hasinger, G., & Aschenbach, B. 1993, in *Isolated Pulsars*, Eds. K. A. Van Riper, R. I. Epstein, & C. Ho (Cambridge: Cambridge), p116.
- Becker, W., Trümper, J., & Ögelman, H. 1993, in *Isolated Pulsars*, Eds. K. A. Van Riper, R. I. Epstein, & C. Ho (Cambridge: Cambridge), p104.
- Bildsten, L. & Epstein, R. I. 1989, *ApJ*, 342, 951.
- Boynton, P. E. 1981, in *IAU Symposium 95, Pulsars*, ed. R. Wielebinski & W. Sieber (Dordrecht: Reidel), p. 279.
- Boynton, P. E. & Deeter, J. E. 1979, in *Compact Galactic X-Ray Sources*, ed. F. K. Lamb & D. Pines (Urbana: University of Illinois), p. 168.
- Brinkmann, W. & Ögelman, H. 1987, *A&A*, 182, 71.
- Brown, G. E. 1988, *Nature*, 336, 519.
- Brown, G. E., Kubordera, K., Page, D., & Pizzochero, P. 1988, *Phys.Rev.D*, 37, 2042.
- Chao, N.-C., Clark, J. W., & Yang, C.-H. 1972, *Nuc.Phys.A*, 179, 320.
- Chau, H. F. & Cheng, K. S. 1993a, *Phys.Rev.B*, 47, 2707
- Chau, H. F. & Cheng, K. S. 1993b, in *Isolated Pulsars*, Eds. K. A. Van Riper, R. I. Epstein, & C. Ho (Cambridge: Cambridge), p35.
- Córdoba, F. A., Hjellming, R. M., Mason, K. O., & Middleditch, J. 1989, *ApJ*, 345, 451.

- Epstein, R. I., & Baym, G. 1988, ApJ, 328, 680.
- Finley, J. P. & Ögelman, H. 1993, in *Isolated Pulsars*, Eds. K. A. Van Riper, R. I. Epstein, & C. Ho (Cambridge: Cambridge), p110.
- Finley, J. P., Ögelman, H., & Kiziloğlu, Ü. 1992, ApJ, 394, L21.
- Friedman, B., & Pandharipande, V. R. 1981, Nuc.Phys.A, 361, 502 (FP).
- Friman, B. L. & Maxwell, O. V. 1979, ApJ, 232, 541.
- Gorenstein, P., Seward, F., & Tucker, W. 1983, Helfand, D. J. 1983, in *IAU Symposium 101, Supernova Remnants and Their X-Ray Emission*, Ed. P. Gorenstein & J. Danziger (Dordrecht: Reidel), p. 1.
- Greenstein, G. 1975, ApJ, 200, 281.
- Halpern, J. P., & Ruderman, M. 1993, ApJ, 415, 286.
- Harding, D. Guyer, R. A., & Greenstein, G. 1978, ApJ, 222, 991.
- Helfand, D. J. 1983, in *IAU Symposium 101, Supernova Remnants and Their X-Ray Emission*, Ed. P. Gorenstein & J. Danziger (Dordrecht: Reidel), p. 471.
- Helfand, D. J., Chanan, G. A., & Novick, R. 1980, Nature, 283, 337.
- Hoffberg, M., Glassgold, A. E., Richardson, R. W., & Ruderman, M. 1970, Phys.Rev.Lett, 24, 775.
- Itoh, N., Kohyama, J., Matsumoto, N., & Seki, M. 1984, ApJ, 285, 304.
- Iwamoto, N. 1980, Phys.Rev.Lett, 44, 1637.
- Jones, P. B. 1990, MNRAS, 243, 257.
- Jones, P. B. 1991, ApJ, 373, 208.
- Kiguchi, M., & Sato, K. 1981, Progr.Theor.Phys.Lett, 66, 725.
- Lattimer, J. M., Pethick, C. J., Prakash, M., & Haensel, P. 1991, Phys.Rev.Lett, 66, 2701.
- Lattimer, J. M. & Swesty, F. D. 1991, Nuc.Phys.A, 535, 331.
- Lattimer, J. M. & Van Riper, K. A., Prakash, M., & Prakash, M. 1993, ApJ425, 802.
- Link, B. & Epstein, R. I. 1991, ApJ, 373, 592 (LE).
- Link, B., Epstein, R. I., & Baym, G. 1993, ApJ, 403, 285 (LEB).
- Link, B., Epstein, R. I., & Van Riper, K. A. 1992, Nature, 359, 616.
- Lorenz, Ravenhall, D. G., & Pethick, C. J. 1993, Phys.Rev.Lett, 70, 379 (1993)
- Maxwell, O. V., Brown, G. E., Campbell, D. K., Dashen, R. F., & Manassah, J. T. 1977, ApJ, 216, 77.
- Migdal, A. B. 1959, Nuc.Phys, 13, 655.
- Miller, M. C. 1992, MNRAS, 255, 129.

- Miller, M. C. 1993, in *Isolated Pulsars*, Eds. K. A. Van Riper, R. I. Epstein, & C. Ho (Cambridge: Cambridge), p153.
- Murray, S. S., Fabbiano, G., Fabian, A. C., Epstein, A., & Giacconi, R. 1979, *ApJ*, 234, L69.
- Negele, J. W. & Vautherin, D. 1973, *Nuc.Phys.A*, 207, 298.
- Nomoto, K. & Tsuruta, S. 1987, *ApJ*, 312, 711.
- Ögelman, H. & Zimmermann, H.-U. 1989, *A&A*, 214, 179.
- Page, D. 1994, *ApJ*, 428, 250.
- Pandharipande, V. 1971, *Nuc.Phys.A.*, 178, 123.
- Pandharipande, V. R., & Smith, R. A. 1975, *Nuc.Phys.A*, 237, 507 (PS).
- Pethick, C. J. & Thorsson, V. 1994, *Phys.Rev.Lett*, in press.
- Pines, D., Shaham, J., Alpar, M. A., & Anderson, P. W. 1980, *Prog.Theor.Phys.Suppl.*, 69, 376.
- Prakash, M., Ainsworth, T. L., & Lattimer, J. M. 1988, *Phys.Rev.Lett*, 61, 2518.
- Pye, J. P., Pounds, K. A., Rolf, D. P., Seward, F. D., Smith, A., & Willingale, R. 1981, *MNRAS*, 194, 569.
- Romani, R. W. 1987, *ApJ*, 313, 718.
- Ruderman, M. 1976, *ApJ*, 203, 213.
- Ruderman, M. 1991, *ApJ*, 366, 261.
- Shibanov, Yu. A., Zavlin V. E., Pavlov, G. G., Ventura, J., & Potekhin, A. Yu. 1993, in *Isolated Pulsars*, Eds. K. A. Van Riper, R. I. Epstein, & C. Ho (Cambridge: Cambridge), p174.
- Shibazaki, N. & Lamb, F. K. 1989, *ApJ*, 346, 808.
- Tuohy, I., & Garmire, G. 1980, *ApJ*, 239, L107
- Van Riper, K. A. 1988, *ApJ*, 329, 339.
- 1991a, *ApJ*, 372, 251.
- 1991b, *ApJS*, 75, 449.
- Van Riper, K. A., Epstein, R. I., & Miller, G. S. 1991, *ApJ*, 381, L47.
- Umeda, H., Shibazaki, N., Nomoto, K., & Tsuruta, S. 1993, *ApJ*, 408, 186 (USNT).
- Wambach, J., Ainsworth, T. L., & Pines, D. 1991, in *Neutron Stars: Theory and Observations*, ed. J. Ventura & D. Pines (Dordrecht: Kluwer), 37.
- Yancopoulos, S., Hamilton, T. T., & Helfand, D. J. 1994, *ApJ*, (in press).

Fig. 1.— Thermal evolution of an FP star of gravitational mass $1.4M_{\odot}$ without frictional heating (*solid curves*) and with heating using the EB (*dashed curves*) and ACP (*dot-dashed curves*) pinning parameters. For each case, the evolution was calculated with “standard” neutrino emissivities and with “accelerated” cooling due to emission from quarks. The *dotted curve* is an isothermal approximation to the standard EB model. A surface magnetic field of 10^{12} G is assumed. Data and upper limits, discussed in the text, are shown. Uncertainties associated with the atmospheric physics and age determinations are shown by the error cross on the right side of each figure (see text). When comparing theoretical curves with data, two factors must be borne in mind. 1) For all pulsars except the Crab, the ages shown correspond to a braking index of 3; an index of 2 gives half the age shown, while an index of 4 give 1.5 times the age shown. 2) The theoretical curves correspond to an $h = 1$ spin-down parameter (see eq. [7]) The heating rate of a given pulsar is proportional to its spin-down parameter (given in Table 2). At late times, the luminosity equals the heating rate, and the curves with heating must be shifted by a factor h in the luminosity. At early times, the required shift can be estimated by the difference between the EB and ACP curves, which differ by a factor of ~ 10 in the heating rate.

Fig. 2.— Same as Fig. 1, for a PS star.

Fig. 3.— Same as Fig. 1 for a BPS star, except accelerated cooling with heating was calculated assuming an isothermal core to save computer time.

Fig. 4.— Evolution of the scaled heating rate, $H(t)t^{3/2}$, normalized to its value at at 10^7 yr (*top panel*), and the inner crust temperature (*bottom panel*).

Fig. 5.— Net heating rates for an FP star from this work (*solid lines*) and from USNT (*dashed lines*) for several pinning models.

Fig. 6.— Steady state surface luminosity as a function of inner crust source rate for FP neutron stars. The luminosity is equal to the source rate along the *dotted line*.

Fig. 7.— Cooling curves for an FP star compared with steady state results (*filled circles*). The logarithm of the source strengths H in erg s^{-1} is shown above the bottom axis. Models calculated assuming isothermality are shown as *dashed lines*.

Figure 5

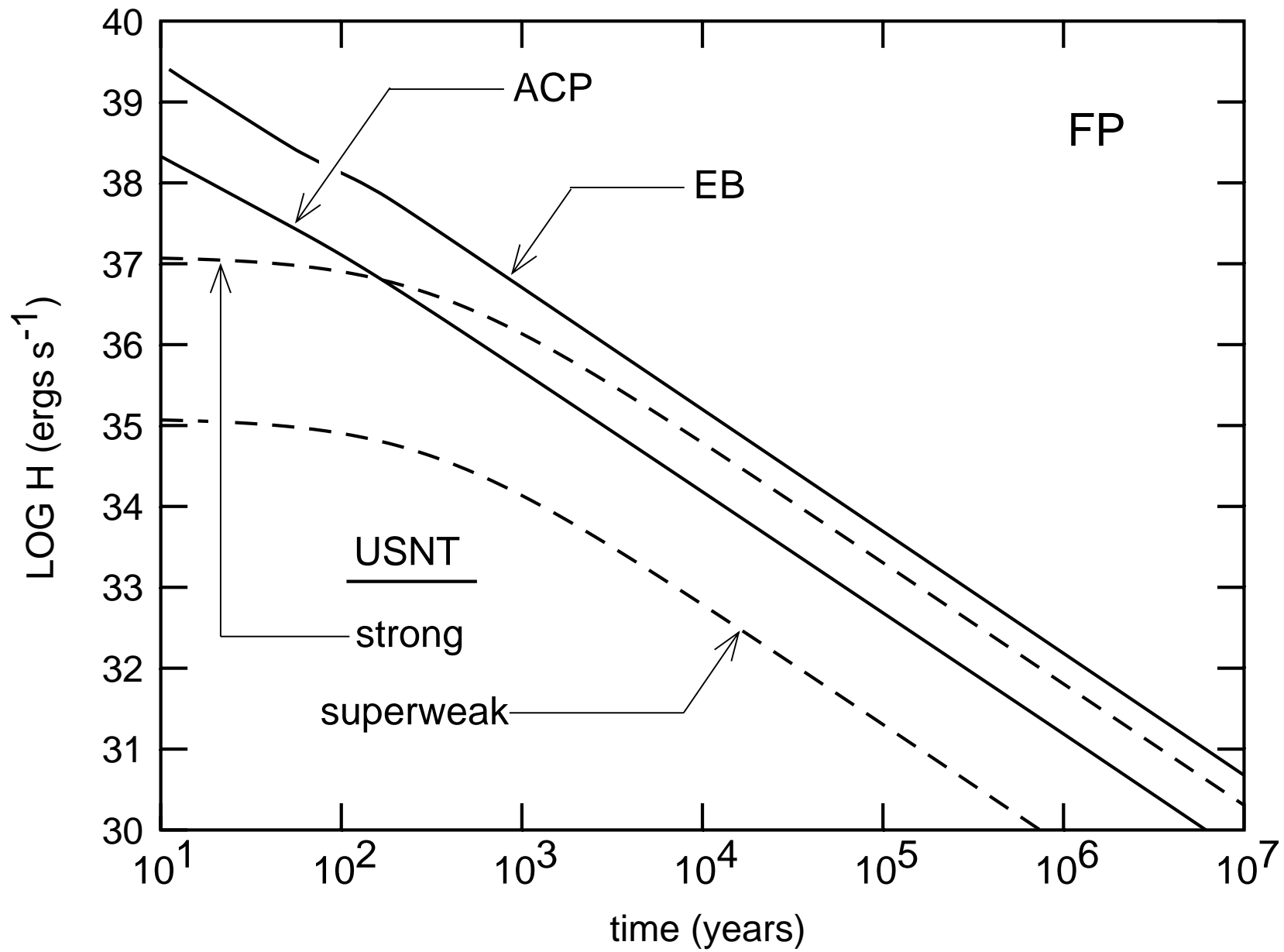


Figure 4

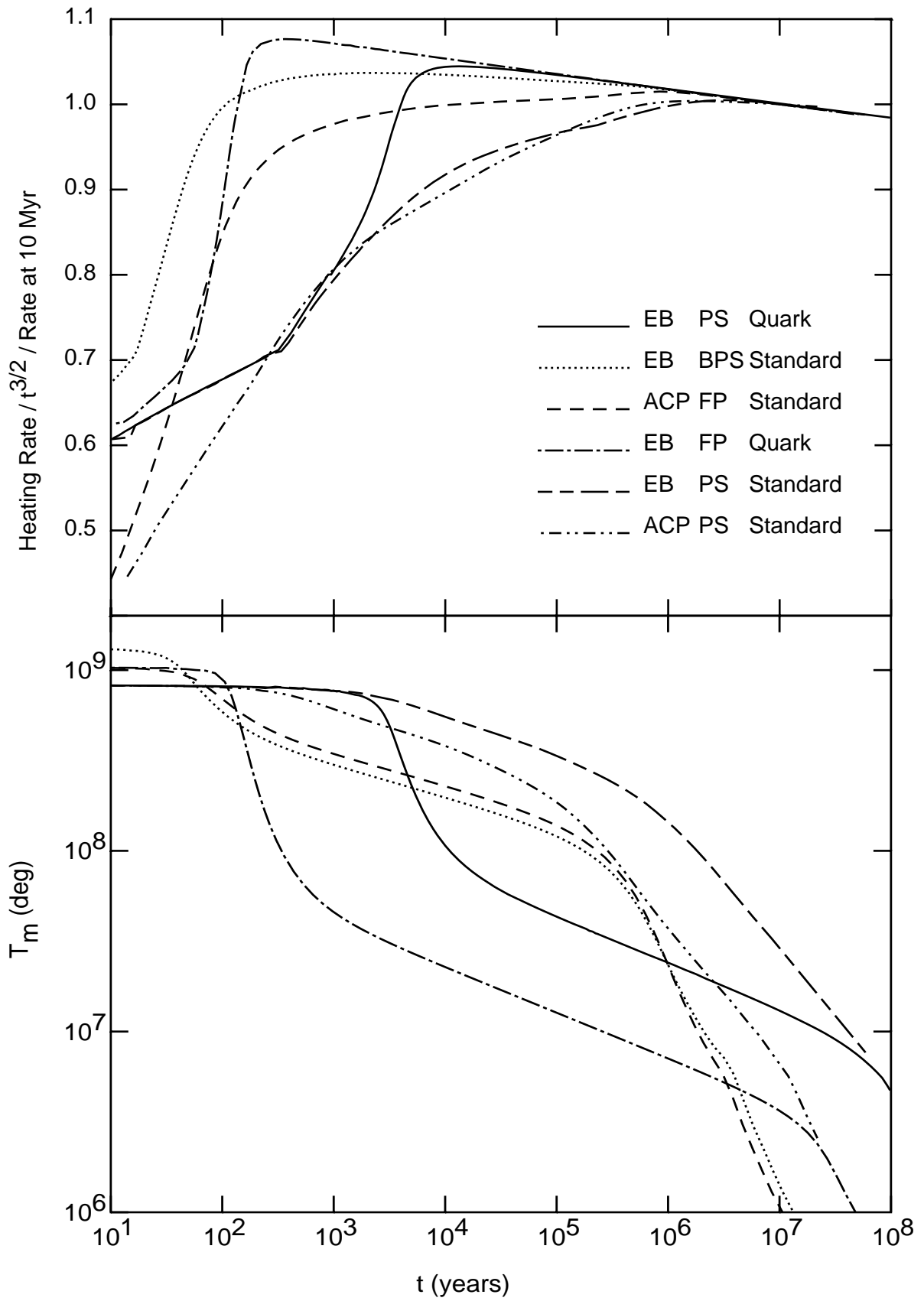
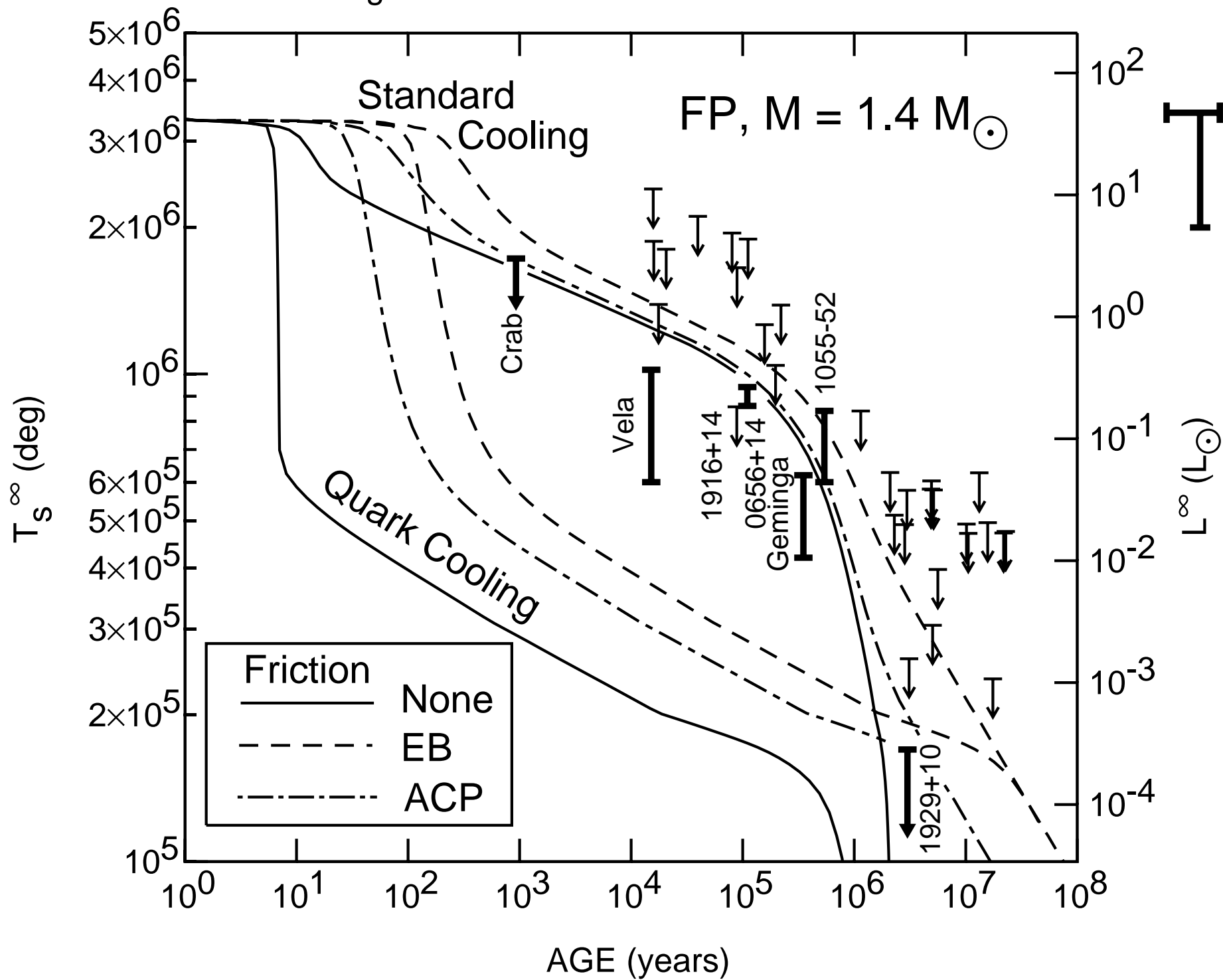


Figure 1



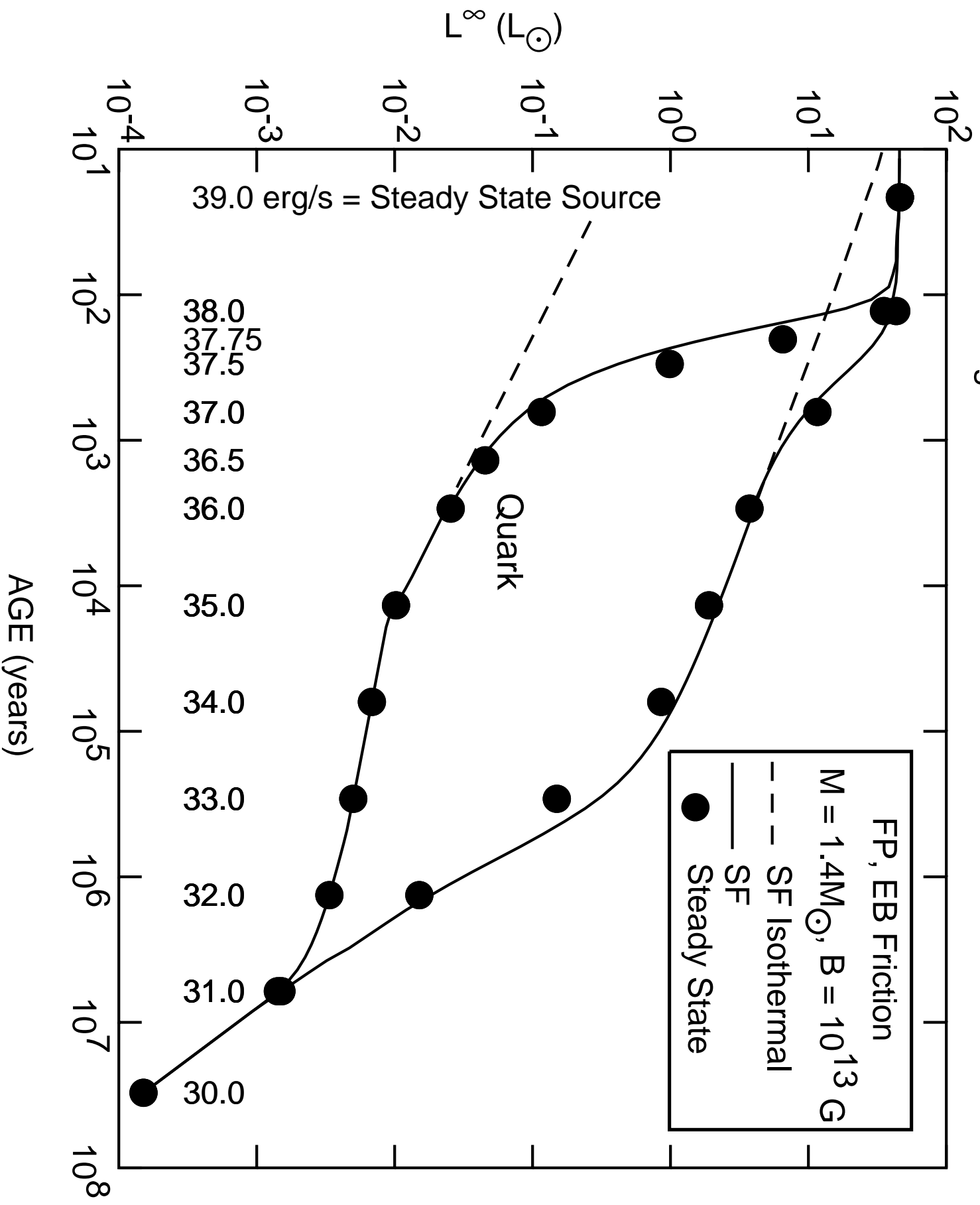


Figure 7

Figure 6

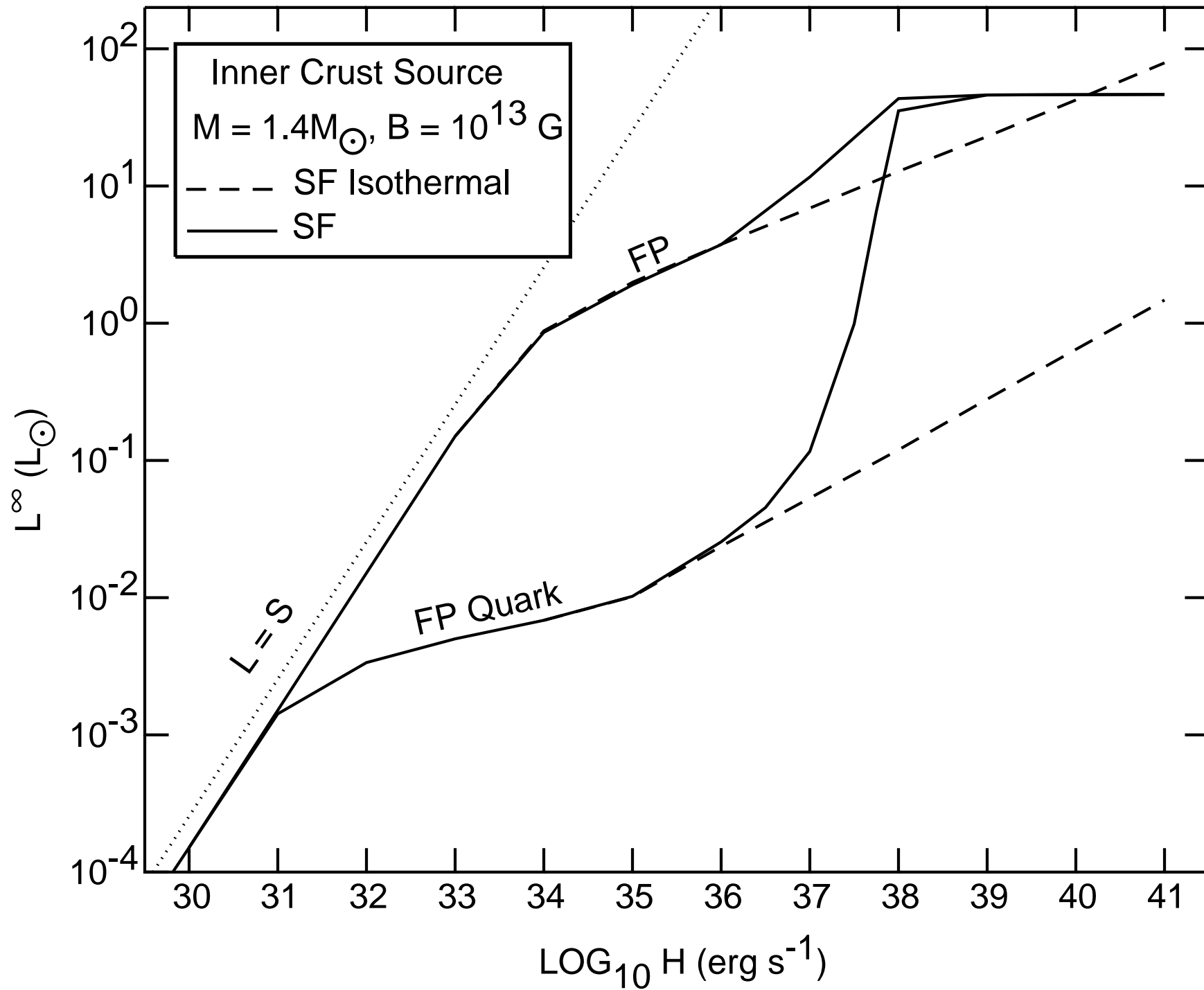


Figure 3

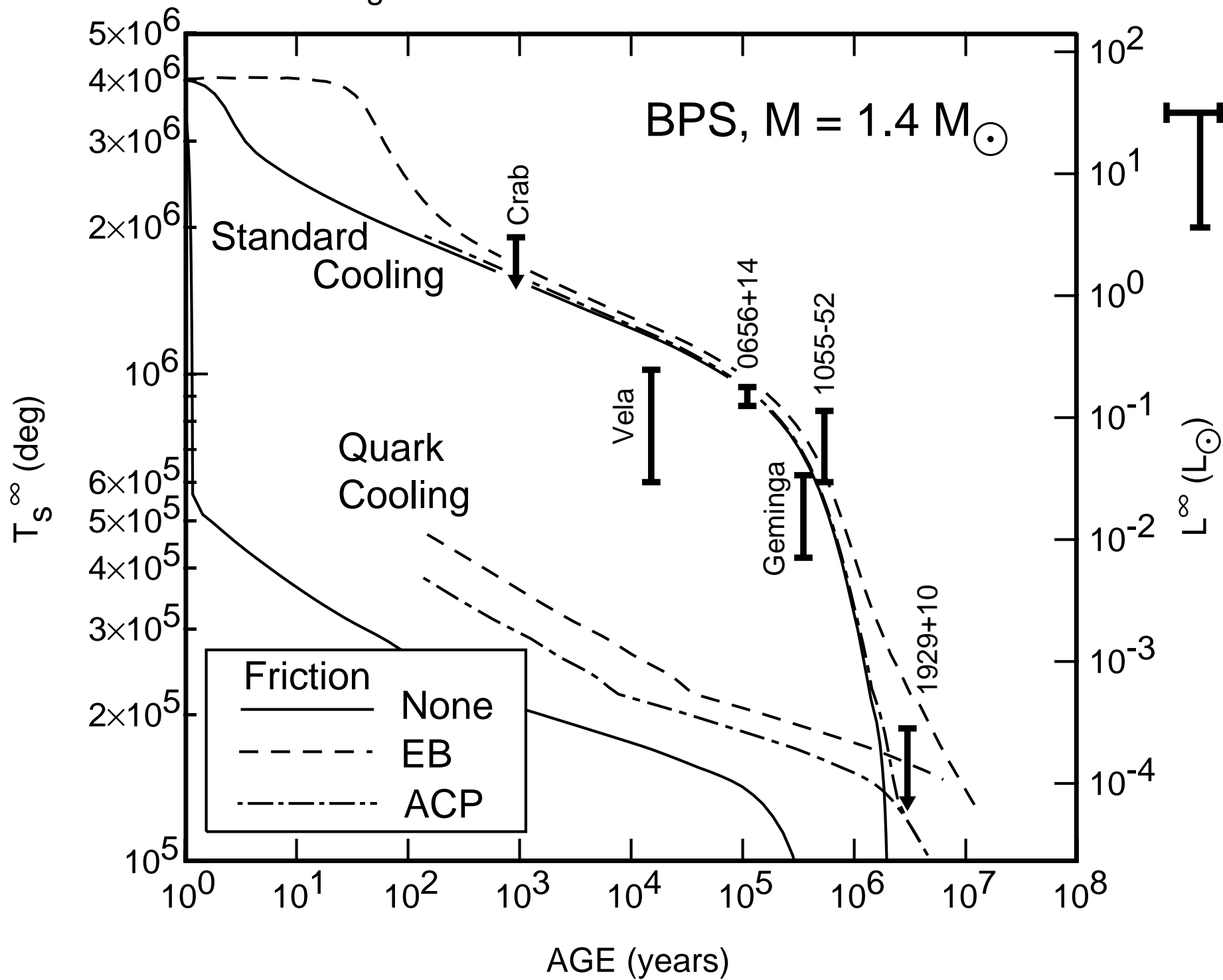


Figure 2

